Polymer 51 (2010) 274–290

Contents lists available at ScienceDirect

Polymer

journal homepage: www.elsevier.com/locate/polymer

# Modeling of melt electrospinning for semi-crystalline polymers

Eduard Zhmayev, Daehwan Cho, Yong Lak Joo*

*School of Chemical and Biomolecular Engineering, Cornell University, Ithaca, NY 14853, USA*

ARTICLE INFO

*Article history:*
Received 1 October 2009
Received in revised form
28 October 2009
Accepted 13 November 2009
Available online 18 November 2009

*Keywords:*
Melt electrospinning
Flow induced crystallization
Nylon-6

ABSTRACT

A comprehensive model for the stable jet region in electrospinning of crystallizing polymer melts has been presented. First, the conventional flow-induced crystallization (FIC) model by Ziabicki was coupled with the non-isothermal melt electrospinning model. The modeled initial jet profiles were compared to digitized experimental images of the stable Nylon-6 melt jet near the spinneret. The final jet diameters were also compared to the average thickness of collected fibers. The results were in good agreement with the flow visualization experiments for various melt temperatures and flow rates. The modeled crystallinity predictions were also in agreement with experimental data from collected fiber mats. Then, a new FIC model that can provide microstructure information, such as crystallite number density and average size, has been proposed and validated under isothermal and non-isothermal conditions in the bulk as well as in the confined geometry of the polymer melt jet in electrospinning. Nylon-6,6 was used as the model polymer in this crystallization study, and the results are in good agreement with the widely-used Ziabicki FIC model.



## 1. Introduction

Understanding crystallization is important to industrial processes because of its close relationship with the observable mechanical properties of the material. Crystallization is an extremely complex stochastic process even when only small molecules are involved. As the scope of the problem is expanded to polymer solutions and finally polymer melts, the complexity becomes staggering. Besides thermodynamic considerations, governing the stability of the crystalline phases, kinetic effects, such as molecular diffusion, have been shown to be of significant importance. Numerous experimental studies have been performed to establish a more thorough understanding of crystallization [1–9]. They have spawned a number of detailed models that can accurately match the overall degree of crystallinity (DOC), however, a substantial gap still exists, especially in the area of understanding the early crystal nucleation process.

The first crystallization model was presented by Kolmogoroff [10], who considered a two-stage process, consisting of nucleation and crystal growth. This model did not find much use at the time due to the lack of experimental data, so a simplified model by Avrami [11] was used exclusively for several decades, and is still widely-used [12]. Avrami linked evolution of the DOC to an overall crystallization rate and the dimensionality of growth. The model works well, but is not predictive, as the crystallization rate changes for each material, process, and set of processing conditions. The advent of differential scanning calorimetry (DSC) enabled the measurement of the crystallization rate at various temperatures, allowing non-isothermal modifications to the Avrami model to be proposed by Ozawa [13] and Nakamura, et al. [14]. Ziabicki [15] proposed a Gaussian in temperature function for the crystallization rate, which mimics the physical maximum at a certain temperature between the glass transition and the melting temperature of the polymer. Hoffman and Lauritzen [16] in their break-through work have been able to address the crystal growth stage in great detail. Their work was based on transition state theory and focused on molecular scale events: a) chain reptation through an entangled network of other polymer chains and b) chain segment surface nucleation, a probabilistic event, signifying the segment realignment to the correct crystallographic configuration. Reptation is an increasing exponential function of temperature, nucleation is a decreasing exponential function of temperature, and the resulting overall growth rate is nearly Gaussian in temperature. This model has shown excellent agreement with polarized optical microscopy (POM) studies [9,17], and is in wide use today. The nucleation process for small molecule systems is thermodynamically controlled and is well predicted by the Becker-Döring nucleation theory [18]. Nucleation can be triggered by formation of a thermodynamically stable embryo due to spontaneous collision of a number of molecules – "homogeneous" nucleation. Alternatively,

* Corresponding author. Tel.: +1 607 255 8591; fax: +1 607 255 9166.
*E-mail address:* ylj2@cornell.edu (Y.L. Joo).

0032-3861/$ – see front matter © 2009 Elsevier Ltd. All rights reserved.
doi:10.1016/j.polymer.2009.11.025

and more likely, a pre-existing foreign particle can become a seed for crystallization. This "heterogeneous" nucleation mechanism is activated by the first attachment of crystallizing material. For larger molecules, such as polymers, stable embryos can also be formed by correct folding of a portion of the long chain. Since mobility of polymers is hindered by their size, macromolecular nucleation is a complex kinetically-controlled process. For dominantly heterogeneous nucleation, one can apply the surface nucleation ideas of Hoffman and Lauritzen. This approach is referred to as the "isokinetic" approximation [14]. In general, the early nucleation stage is poorly understood due to the time and length-scales involved not being easily accessible by modern experimental techniques, which has made it an appealing subject to a number of micro scale simulation investigations [19]. However, the process is extremely computationally expensive and so far the results cannot be directly applied to continuum level modeling or macro scale crystallinity predictions.

The next challenging area is the phenomenon of flow-induced crystallization (FIC), in which strong uniaxial forces elongate the polymer chains and consequently drastically alter the crystallization morphology and kinetics of nucleation and crystal growth. Despite numerous experimental studies that have evidenced this phenomenon [9,20–26], no clear understanding and thus no predictive fundamental theory on these effects exists. Phenomenologically, Ziabicki [15] proposed to incorporate the effect of flow as an empirical enhancement factor to the overall crystallization rate. This enhancement factor can be linked to internal stresses and experimental birefringence data via the stress-optical rule [27]. This approach can fit experimental data well but is not predictive, as the parameters have to be determined for the particular process, material, and conditions. The Doufas and McHugh model [28] incorporates FIC in a similar empirical way and links the enhancement to the trace of the internal stress tensor. This model includes several coupling parameters, which allow for excellent experimental data fitting capabilities. However, the model is still not predictive. Some of the coupling parameters do not have a specific physical meaning and are process and condition dependent. In a previous communication [29], we have presented an alternative approach to modeling of FIC. The nucleation and growth events have been separated, because the microstructure details, such as the number of crystals and their sizes, could be important to the mechanical properties of the resulting material. Furthermore, flow can affect both nucleation and growth stages and to different extents.

In the present study we will provide further validation for this crystallization model in a practical application to melt electrospinning process. Electrospinning utilizes applied electric field to accelerate and drastically elongate a charged fluid jet. It has been shown experimentally that electrospun nano-scale fibers can be readily produced from polymer solutions [30–32] and more recently even melts [33–37]. Nanofibers, with high surface area to mass ratios, are extremely attractive for use in high performance filtration, biological and biomedical fields, and in the chemical industry [30,31,38]. Alternative technologies for nanofiber fabrication include multi-stage conventional mechanical spinning and melt blowing. Conventional fiber spinning is typically able to produce fibers $\sim$10–100 μm in diameter, and a second re-draw step is then utilized to thin the fibers further [38]. Melt blowing can produce sub-micron fibers in a one-stage process, however, due to the underlying driving mechanism, the fiber attenuation is inherently relatively small, and thus very small orifices are required [39]. Effective deformation by the electric field in melt electrospinning results in rapid attenuation, high internal stresses, and consequently rapid development of molecular orientation. As a result, significant FIC can be observed in many melt-electrospun fibers, which makes this process an excellent platform for the modeling of FIC.

In this publication, a continuum level model for the stable jet region in electrospinning of crystallizing polymer melts, including FIC, is presented. We utilize a previously developed non-isothermal model for amorphous polymer melts in electrospinning [37], and fully couple crystallization equations with momentum, continuity, and energy equations, Gauss' law, and non-isothermal viscoelastic constitutive models. The thin filament approximation is applied as appropriate to this fiber system. The theoretical predictions are validated with experimental data and by comparison to the Ziabicki FIC model.

## 2. Modeling procedure

### 2.1. Melt electrospinning process

In polymer melt electrospinning, a charged fluid jet undergoes rapid elongation and thinning under the influence of a strong applied external electric field. In the initial thinning region, $\sim 5R_0$ ($R_0$ is the radius of the nozzle), the fluid jet experiences the fastest thinning resulting in a buildup of internal stresses and alignment of polymer chains in the axial direction. As the jet temperature decreases to below the polymer melting point, $T_m$, the viscosity increases, the thinning rate decreases, and the jet profile becomes nearly cylindrical. By this point, the jet has become so thin that the radial stress and temperature profiles are nearly uniform. Since the in-flight residence time is extremely short, $\sim$1 ms, thermally-induced crystallization is not significant. Even the fastest crystallizing polymers typically have crystallization half-times on the order of seconds. However, the large internal stresses and nearly perfect chain alignment can result in the onset of FIC that occurs on a much shorter time scale than thermal crystallization. In the following sections, a new model specifically tailored to the crystallization process in electrospinning is discussed.

### 2.2. Governing equations for flow-induced crystallization

As discussed above, most of the FIC models to-date are based on a non-isothermal version of the Avrami equation, proposed by Nakamura [14]:

$$\theta = 1 - \exp\left\{ - \left( \int_0^t K dt' \right)^n \right\}, \tag{1}$$

where $\theta$ is the DOC, defined as the ratio of the volume fraction crystallinity to the maximum obtainable crystallinity, $n$ is the dimensionality of growth, and $K$ is the non-isothermal crystallization rate. For non-isothermal flow, it is convenient to re-write this equation in differential form (Lagrangian coordinates):

$$v \cdot \nabla \theta = nK(1-\theta)\left[ \ln\left( \frac{1}{1-\theta} \right) \right]^{(n-1)/n}, \tag{2}$$

where $v$ is the average fluid velocity, and $\nabla$ is the spatial gradient. The crystallization rate, $K$, is given by an empirical equation from Ziabicki [15]:

$$K(T, f_a) = K_{\max} \exp\left\{ -4\ln 2 \left( \frac{T - T_{\max}}{T_D} \right)^2 \right\} \exp\left\{ C f_a^2 \right\}, \tag{3}$$

where $K_{\max}$ is the maximum crystallization rate at the corresponding temperature $T_{\max}$, and $T_D$ is the crystallization peak half-width. The flow effects are incorporated by the addition of

a molecular orientation function $f_a$, with $C$ being the stress-crystallization coupling coefficient that, in general, may be a function of temperature:

$$f_a = \frac{\Delta\alpha}{\Delta\alpha_i} = \frac{-C_{op}(\tau_{p,zz} - \tau_{p,rr})}{\Delta\alpha_i}, \tag{4}$$

$$C = \frac{C_1 + C_2(T_m - T)}{(T_m - T)^3}. \tag{5}$$

The molecular orientation function $f_a$, is defined as the ratio of amorphous birefringence, $\Delta\alpha$, and a material constant amorphous intrinsic birefringence, $\Delta\alpha_i$. The amorphous birefringence in uniaxial extension can be linked to the first normal stress difference, $\tau_{p,zz} - \tau_{p,rr}$, by the stress-optical law, with $C_{op}$ being the stress-optical coefficient. Note that $C$ is singular at $T = T_m$, which is not a problem for most processes because the crystallization rate is typically negligible at this temperature. In electrospinning, significant molecular alignment is present from the very onset of crystallization, and thus $C$ should be taken to be constant, or alternatively, the following functionality is proposed:

$$C = C_x \exp\left\{-\left(\frac{T - T_{\max}}{T_D}\right)^2\right\}. \tag{6}$$

Doufas and McHugh [28] have approached the problem in a similar manner, but have linked the molecular orientation function directly to the trace of the internal stress tensor with a different set of coupling coefficients.

One important goal of the present study is to bring additional microscopic detail into this continuum level model, and thus the formulation begins with the comprehensive classical crystallization equation by Kolmogoroff [10]:

$$\theta = 1 - \exp\left\{-\xi \int_0^t \left[\left(\int_s^t G(u)du\right)^n \frac{dN}{ds}\right] ds\right\}, \tag{7}$$

where $\xi$ is the shape factor that depends on morphology of the crystal growth, $G$ is the growth rate normal to the phase transition front, and $N$ is the crystal number density. The growth rate can be measured in quiescent POM experiments and fit to the Hoffman-Lauritzen model [16]:

$$G(T) = G_0 \exp\left\{-\frac{U^*}{R_{ig}(T - T_\infty)}\right\} \exp\left\{-\frac{\kappa_G T_m^2 (1 + T/T_m)}{2T^2(1 - T/T_m)}\right\}, \tag{8}$$

where $R_{ig}$ is the ideal gas constant, $T_\infty$ is the temperature at which molecular motion stops (glass transition temperature in the present model), and $T_m$ is the equilibrium melting temperature. The three fitting constants are: the growth rate pre-factor $G_0$, the equilibrium activation energy of chain motion $U^*$, and the surface nucleation constant $\kappa_G$. The transient crystal number density can also be theoretically obtained from POM studies, but this measurement is difficult and not very accurate. Alternatively, DSC data for the overall crystallization rate can be utilized to back-calculate the crystal density. The procedure outlined by Lamberti [40] results in the following equation:

$$N(T) = N_0 \exp\left\{-3\frac{(\kappa_T - \kappa_G) T_m^2 (1 + T/T_m)}{2T^2(1 - T/T_m)}\right\}, \tag{9}$$

where the two new fitting constants are: the pre-factor $N_0$, and the nucleation constant $\kappa_T$. This expression assumes the instantaneous heterogeneous nucleation mechanism, but allows for continuous adjustment of the crystal number density due to activation of smaller embryos if/when the process temperature decreases. Equations (7)–(9) now form the basis of the refined quiescent crystallization model.

The modifications for FIC are added to each of the equations by considering the flow effects on molecular scale events leading to crystallization: 1) enhancement of chain reptation and 2) enhancement of chain segment nucleation. Let us first consider the reptation enhancement. We hypothesize that flow affects chain motion through segment orientation, thus reducing the molecular drag:

$$\zeta(\phi) = \sqrt{\zeta_\perp^2 \sin^2\phi + \zeta_\parallel^2 \cos^2\phi}, \tag{10}$$

where $\zeta_\perp$ and $\zeta_\parallel$ are friction coefficients for motion of rod-like chain elements (Kuhn segments) in the normal and parallel directions with respect to their long axis, respectively, and $\phi$ is the average segment orientation relative to alignment direction, which can be found from the macroscopic order parameter, $S$:

$$S \equiv \frac{3\cos^2\phi - 1}{2}. \tag{11}$$

The order parameter, $S$, is calculated on the continuum level from the configuration tensor $<\boldsymbol{QQ}>$, which for a particular constitutive model (in this case Giesekus model) can be found from the internal stress tensor, $\boldsymbol{\tau_p}$, [41]:

$$S \equiv \sqrt{\frac{3}{2}(\boldsymbol{S} : \boldsymbol{S})}, \tag{12}$$

$$\boldsymbol{S} \equiv \frac{\langle \boldsymbol{QQ} \rangle}{tr\langle \boldsymbol{QQ} \rangle} - \frac{1}{3}\boldsymbol{\delta}, \tag{13}$$

$$\langle \boldsymbol{QQ} \rangle = \boldsymbol{\delta} - \frac{De}{1 - \beta}\boldsymbol{\tau_p}, \tag{14}$$

where $\boldsymbol{\delta}$ is the unit tensor, $De$ is the Deborah number representing importance of polymer relaxation time with respect to a flow time scale, and $\beta$ is the ratio of solvent to zero-shear-rate viscosity. The reptation enhancement is incorporated as factor $f_R$:

$$f_R(S) = \frac{\zeta_{S=0}}{\zeta_S} = \sqrt{\frac{1 + 2\left(\zeta_\perp/\zeta_\parallel\right)^2}{(1 + 2S) + (2 - 2S)\left(\zeta_\perp/\zeta_\parallel\right)^2}}, \tag{15}$$

which will appear three times due to: a) molecular friction dependence implicitly imbedded in $G_0$ pre-factor [16], b) same dependence imbedded in $N_0$, and $c$) enhancement of the activation energy of motion, $U^*$:

$$\exp\left\{-\frac{U^*}{kT}\right\} \sim \zeta. \tag{16}$$

We now return to the chain segment nucleation enhancement. We hypothesize that flow-induced ordering in the melt phase decreases the entropic penalty of the phase transition, thus effectively elevating the melting point:

$$T_m = \frac{\Delta h}{\Delta s}, \tag{17}$$

where $\Delta h$ and $\Delta s$ are enthalpy and entropy changes due to phase transition, respectively. We propose that *relative* chain segment alignment decreases melt entropy, but the order of this dependence, $m$, is not known *a priori* and could range from 2 for short

range interactions to some larger value if long range order is of importance. Alignment elevates the melting point from its equilibrium value, $T_{m0}$, at $S=0$ to some larger value, $T_{m\infty}$, at $S=1$, and is incorporated in the model as nucleation enhancement factor, $f_T$:

$$f_T(S) = \frac{1-S^m}{T_{m0}} + \frac{S^m}{T_{m\infty}}. \tag{18}$$

The new equations for growth rate and crystal number density are then:

$$G(T,S) = G_0 f_R^2 \exp\left\{-\frac{U_0^*}{R_{ig}(T-T_\infty)}\right\}\exp\left\{-\frac{\kappa_G T_{m0}^2(1+Tf_T)}{2T^2(1-Tf_T)}\right\}, \tag{19}$$

$$N(T,S) = N_0 f_R \exp\left\{-3\frac{(\kappa_T-\kappa_G)T_{m0}^2(1+Tf_T)}{2T^2(1-Tf_T)}\right\}. \tag{20}$$

This model includes three new adjustable parameters: $\zeta_\perp/\zeta_\parallel$, $m$, and $T_{m\infty}$, which can be fitted, found from independent experiments, or even determined from separate micro scale simulations.

For electrospinning simulations, several simplifying approximations can be employed. Due to the small jet diameter in crystallization region, the radial temperature and stress variation is assumed to be negligible. Based on experimental evidence [42] and other modeling studies [43], the strong elongational forces in electrospinning should result in primarily rod-like fibrillar crystalline structures. With these assumptions, Equation (7) is rewritten in differential form:

$$v\frac{d\theta}{dz} = (1-\theta)N\left[2A_f G\right], \tag{21}$$

where $z$ is axial (elongation) direction and $A_f$ is the rod cross-sectional area ($\sim 10^{-16}$ m$^2$).

### 2.3. Governing equations for modeling of electrospinning

The crystallization model from the preceding section is coupled with the previously developed model for electrically driven free surface flow in electrospinning [37]. The model was developed for the stable jet region and the supporting experiments purposefully suppressed the whipping motion of the jet. The motivation for this treatment lies in experimental observations that a significant fraction of thinning, particularly for melts, can occur in the stable jet region. Thus a reliable model for the stable jet is required and can serve as the basis for further stability analysis to address the axisymmetric and whipping instabilities. Furthermore, for certain applications requiring careful fiber alignment, whipping motion reduction by electric field manipulation may be desired. In fact, due to low electrical conductivity and high jet rigidity of polymer melt systems, the whipping motion suppression is often practically unavoidable.

Conservation of momentum for the stable jet in electrospinning can be represented by the following equation:

$$\mathrm{Re}v v' = G_N + \frac{\left(R^2(\tau_{zz}-\tau_{rr})\right)'}{R^2} + \frac{R'}{CaR^2} + F_e\left[\sigma\sigma' + \beta_E E_t E_t' + \frac{2\sigma E_t}{R}\right], \tag{22}$$

where $Re$ is the Reynolds number (inertia force/viscous force), $v$ is the average axial jet velocity, $G_N$ is the Gravity number (gravity force/viscous force), $R$ is the jet diameter, $\tau_{zz}$ and $\tau_{rr}$ are the total axial and radial normal stresses, Ca is the Capillary number (viscous force/surface tension), $F_e$ is the electrostatic force parameter (electrostatic force/viscous force), $\sigma$ is the surface charge density, $\beta_E$ is the dielectric constant ratio, $E_t$ is the component of the electric field tangential to the jet surface, and the prime symbol denotes derivative with respect to the axial coordinate. For further details of the model, definitions of the dimensionless numbers and electrostatic terms, and other conservation equations, the reader is directed to our previous publication [37].

In the previous work, the Giesekus constitutive model was utilized to capture the viscoelastic behavior of polymer melts and the model predictions were validated with experiments on slowly-crystallizing polylactic acid (PLA). Here, we provide further results on comparison to electrospinning experiments of fast-crystallizing Nylon-6 and for the model predictions when exponential version of the Phan-Thien and Tanner (PTT) constitutive model [41] is used (with slip parameter set to 0). This version of the PTT model is known to mimic the behavior of polymer melts in extensional flow better than the Giesekus model [44]. The non-isothermal PTT model is represented by the following equations, and the Giesekus model is shown for comparison:

$$\tau_{zz} = \tau_{p,zz} + 2\beta f_v v', \tag{23}$$

$$\tau_{rr} = \tau_{p,rr} - \beta f_v v', \tag{24}$$

Non-isothermal PTT model:

$$\frac{De\,\Gamma}{\Theta+\Gamma}f_v\left(v\tau_{p,zz}' - 2v'\tau_{p,zz} - \frac{v\tau_{p,zz}\Theta'}{\Theta+\Gamma}\right) + \tau_{p,zz}\exp\left\{\frac{\varepsilon_v\tau_{p,zz}}{1-\beta}\left(\frac{De\,\Gamma}{\Theta+\Gamma}\right)\right\} = 2(1-\beta)f_v v', \tag{25}$$

$$\frac{De\,\Gamma}{\Theta+\Gamma}f_v\left(v\tau_{p,rr}' + v'\tau_{p,rr}\right) + \tau_{p,rr}\exp\left\{\frac{\varepsilon_v\tau_{p,zz}}{1-\beta}\left(\frac{De\,\Gamma}{\Theta+\Gamma}\right)\right\} = -(1-\beta)f_v v', \tag{26}$$

Non-isothermal Giesekus model:

$$\tau_{p,zz} + \frac{De\,\Gamma}{\Theta+\Gamma}\left(\frac{\alpha\tau_{p,zz}^2}{(1-\beta)} + f_v\left[v\tau_{p,zz}' - 2v'\tau_{p,zz} - \frac{v\tau_{p,zz}\Theta'}{\Theta+\Gamma}\right]\right) = 2(1-\beta)f_v v', \tag{27}$$

$$\tau_{p,rr} + \frac{De\,\Gamma}{\Theta+\Gamma}\left(\frac{\alpha\tau_{p,rr}^2}{(1-\beta)} + f_v\left[v\tau_{p,rr}' + v'\tau_{p,rr}\right]\right) = -(1-\beta)f_v v', \tag{28}$$

where $\tau_{p,zz}$ and $\tau_{p,rr}$ are the normal axial and radial polymeric stress components, respectively, $\beta$ is the ratio of solvent to zero-shear-rate viscosity, $f_v$ is the rheological shift factor representing the temperature dependence of the zero-shear-rate viscosity and relaxation time, $\Theta$ is dimensionless temperature, $\Gamma$ is the ratio of characteristic temperature scales used in the non-dimensionalization and defined in [37], $\varepsilon_v$ is the PTT parameter allowing for extensional viscosity thinning, and $\alpha$ is the Giesekus mobility parameter. The rheological shift factor is affected by crystallization and this dependence has been incorporated empirically following Patel, et al. [45]:

$$f_v(\Theta,\theta) = \exp\left[\frac{\Delta H}{R_{ig}\Delta T_{Rh}}\left(\frac{1}{\Theta+\Gamma} - \frac{1}{\Gamma}\right) + 4\theta^2\right], \tag{29}$$

where $\Delta H$ is the activation energy of flow, and $\Delta T_{Rh}$ is the temperature change necessary to substantially alter the rheological properties of the fluid. Equation (29) assumes Arrhenius temperature dependence of viscosity and the relaxation time. As the temperature approaches the glass transition $T_g < T < T_g + 50$, the

rheological shift factor is better represented by the sharper dependence of Williams-Landel-Ferry (WLF) equation:

$$f_v(\Theta,\theta) = \exp\left[\frac{-C_1\Delta T_{Rh}\Theta}{C_2+\Delta T_{Rh}\Theta}+4\theta^2\right], \tag{30}$$

where $C_1$ and $C_2$ are the WLF parameters.

Since phase transition was not considered in the previous work, we also show the energy equation that includes the additional energy source term (last term):

$$Pé\, v\Theta' = Na\, v'(\tau_{zz}-\tau_{rr}) - 2Bi_L\frac{(\Theta-\Theta_\infty)}{R} - h_f v\theta', \tag{31}$$

where *Pé* is the Peclét number which relates forced convection to heat conduction, *Na* is the Nahme-Griffith number which is the characteristic temperature rise due to viscous heating divided by the temperature change necessary to substantially alter the rheological properties of the fluid, and $Bi_L$ is the local Biot number – the ratio of the internal thermal resistance in the jet to the boundary layer thermal resistance in the surrounding cooling air:

$$Bi_L \equiv Bi\left(\frac{v}{R^2}\right)^{1/3}\left(\frac{1+(8v_{air}/v)^2}{1+(8v_{air})^2}\right)^{1/6}, \tag{32}$$

where $v_{air}$ and $v$ are the speed of the cooling air and cross-sectional average axial fluid velocity, respectively. All of these dimensionless groups are explained in more detail in our previous work [37]. Finally, $h_f$ is the dimensionless heat of fusion:

$$h_f \equiv \frac{\rho\Delta H_f R_0 V_0 \varphi_\infty}{kT_0}, \tag{33}$$

where $\rho$ is the fluid density, $\Delta H_f$ is the heat of fusion (negative for crystallization), $R_0$ is the nozzle radius, $V_0$ is the jet velocity at the nozzle, $\varphi_\infty$ is the maximum obtainable crystallinity, $k$ is the thermal conductivity, and $T_0$ is the jet temperature at the nozzle.

### 2.4. Numerical solutions

The current model has been formulated as an initial value problem of six coupled first-order ODEs and has been solved numerically using a 4th order Runge-Kutta method with adaptive step size control. The code was based on numerical recipies by Press, et al. [46]. The results of the calculations are presented in the form of the calculated jet radius, elongational viscosity, temperature, and crystallinity profiles. The jet radius profiles and final crystallinity values can be directly compared to experimental results.

## 3. Experimental procedure and model parameters

### 3.1. Melt electrospinning setup and procedure

The melt electrospinning experimental setup and procedure have been described in detail in our previous publication [37]. However, electrospinning of Nylon-6 melt requires higher temperatures than polylactic acid, considered in the previous work, and thus modifications to the heating chamber have been performed to allow for higher temperatures and more uniform temperature distribution. The heater dimensions were minimized so as to allow for rapid change of experimental conditions needed in the optimization process. Special considerations had to be made to electrically isolate the heating element and the thermocouple from the high voltage source as well as shield them from the strong electric field used in the process. The latest generation of the heating system is shown in Fig. 1. The heating element is embedded in a ceramic medium and surrounded by a grounded stainless steel enclosure, which acts as a Faraday cage and shields the electric field effects. The region between the enclosure and the syringe containing the polymer is occupied by a custom-machined cylindrical piece made of highly dielectric ceramic MACOR, manufactured by Corning, Inc., which electrically isolates the Faraday cage from the charged syringe. The nozzle-side of the MACOR cylinder has only a small opening (large enough for a 17 gauge needle) to minimize the heat losses.

The Nylon-6 pellets used in this work have been provided by Hyosung, Inc., Korea, and have a melt flow index (MFI) of 3. Prior to electrospinning, Nylon-6 pellets were dried at 120 °C for 20 h and immediately transferred to a preheated syringe. The humidity was controlled by a de-humidifier to minimize the moisture absorbed by the polymer and prevent bubble formation in the melt. The pellets were placed in a 5 ml syringe and heated for half an hour at 250 °C prior to spinning to ensure complete and uniform melting. The micro-flow controller fed the Nylon melt through a 17 gauge needle with a flow rate of 0.02 ml/min. The potential difference and distance between the nozzle and the collector were 20 kV and 0.1 m, respectively. To suppress the whipping motion for comparison with the stable jet modeling, as previously discussed in [37], the charged melt jet was spun without the heated spinning chamber and finally collected on a water-cooled copper collector.

The predicted simulation results are compared with experiments in two different ways. First, the initial jet radius profiles are collected by focusing a high speed camera (MotionPro HS-3, Redlake) on the spinneret and a section of approximately $10R_0$ into the spinning region and recording a close-up high speed (1000 to 5000 frames per second) movie. For best image quality, the aperture of the lens was reduced to its minimum and rear illumination was provided by a 60 W lamp. The images were digitized using Redlake imaging software and analyzed with ImageJ software. Secondly, the experimental measurements of the final fiber diameters resulting from thinning only in the stable region (no thinning due to whipping motion) were compared with predicted final stable jet diameter. The jet whipping motion was suppressed by maintaining the cooling air temperature at 25 °C, below the glass transition point of Nylon-6. The resulting fiber mat was inspected in a LEICA 440 scanning electron microscope (SEM) and the images were analyzed to determine the fiber sizes and size distribution. Crystallinity of the fibers mats was characterized by performing DSC scans and obtaining wide angle X-ray diffraction (WAXD) patterns. The DSC studies were performed using the Modulated Differential Scanning Calorimeter, TA Instruments Q1000, at the Cornell Center for Materials Research (CCMR), and samples of 3–11 mg were heated from 25 to 300 °C at heating rates between 2.5 and 60 °C/min. Room temperature WAXD studies were performed using a Theta-Theta Diffractometer, Scintag, Inc., in continuous scanning mode, with 0.02° step size, 3°/min scan rate, and in the region of $2\theta = 5$ to 40°. The Fourier transform infrared spectroscopy (FTIR) spectra of the samples in the range from 800 to 1600 $cm^{-1}$ with a 4 $cm^{-1}$ resolution were measured to verify the types of crystals.

### 3.2. Fluid characterization

Two polymers were used in the study: Nylon-6 and Nylon-6,6. Electrospinning experiments were only carried out with Nylon-6 and the experimental jet profiles are compared to simulations. In the absence of reliable experimental crystallization data and parameters for Nylon-6, we have resorted to a well studied Nylon-6,6 as a polymer of choice for the validation of this crystallization

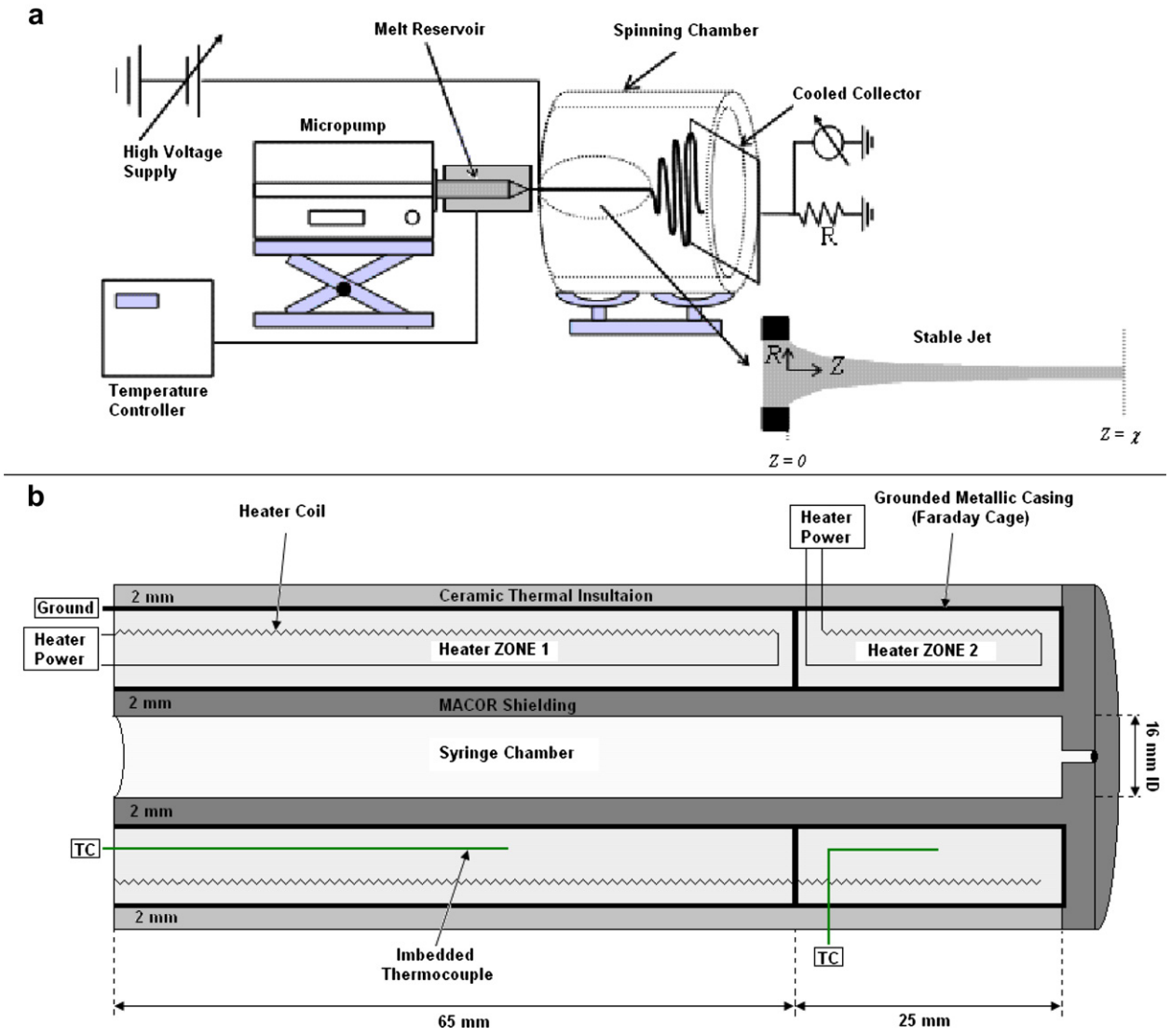


**Fig. 1.** Schematic of the melt electrospinning setup.

model, with the expectation that the crystallization dynamics should be qualitatively similar to those of Nylon-6. Since Nylon-6,6 has a significantly higher melting point than Nylon-6, we have not yet been able to electrospin it due to heater limitations. The theoretical model presented in this paper requires a number of physical properties for the polymers at hand, summarized in Table 1. A number of these properties were measured and others were taken from literature.

The oscillatory rheological measurements for Nylon-6 were performed at 250 °C using parallel plate geometry. The results and the fit to the Giesekus constitutive model are shown in Fig. 2. The current fitting procedure does not always produce a unique set of parameters. Ideally, the relaxation time, $\lambda$, should be found independently from the storage modulus, $G'$, (which is measured concurrently with the shear viscosity) using the following relation:

$$\lambda = \frac{\Psi_{01}}{2\eta_p} = \frac{\lim_{\gamma\to 0}\Psi_1}{2\eta_p} = \frac{\lim_{\omega\to 0}\frac{2G'}{\omega^2}}{2\eta_p}, \tag{34}$$

where $\Psi_1$ is the first normal stress coefficient and $\Psi_{01}$ is its low shear limit, $\omega$ is the oscillatory frequency, and $\eta_p$ is the polymeric contribution to zero-shear-rate viscosity. Unfortunately, it is difficult to obtain good data for Nylons due to their high melting point, especially in the low shear-rate regime, as manifested by the hump in the viscosity plot in Fig. 2. The currently available data does not provide a constant $G'$ in the limit of low oscillation frequency, and the in-house rheometers cannot be used at temperatures above 180 °C. With better data, it would be possible to eliminate one of the fitting parameters and obtain a unique set of properties, but in the mean-time we will use the parameter set reported in Table 1.

In the previous publication [29], it was discussed that the Ziabicki crystallization half-width was modified from the typical value of 313 K found in literature [27] in order to match the quiescent crystallization profile predicted by the Kolmogoroff model with its corresponding parameters [43]. The fit of the two quiescent models with the modified parameters (see Table 1) is shown in Fig. 3.

Finally, it was of interest to compare the model behavior when the WLF model is used for the calculation of the rheological shift factor. To the authors' knowledge, reliable experimental WLF parameters for Nylon-6 and Nylon-6,6 have not been reported, however, Meerveld, et al. [43], reports fitted $C_1$ and $C_2$ values for

**Table 1**
Material properties of Nylon-6 and Nylon-6,6 used in the current study.

| Properties | Nylon-6 | Nylon-6,6 |
|---|---|---|
| Melt density, $\rho$ (kg/m$^3$) | 1000 [47] | 1000 [27] |
| Heat capacity, $C_p$ (J/kg K) | 2553[a] | 2553 [27] |
| Thermal conductivity, $k_T$ (W/m K) | 0.245 [47] | 0.209 [27] |
| Dielectric constant ratio, $\varepsilon/\varepsilon_0$ | 3.2 [48] | 3.2 [48] |
| Surface tension, $\gamma$ (N/m) | 0.030[a] | 0.030 [27] |
| Relaxation time, $\lambda$ (s) | 0.025 @ 250 °C | 0.001 @ 290 °C |
| Giesekus mobility factor, $\alpha$ | 0.04 | 0.4 [27] |
| PTT extensional thinning parameter, $\varepsilon_v$ | 0.015 [22] | 0.015 [22] |
| Activation energy of flow, $\Delta H/R_{ig}$ (K) | 6600[a] | 6600 [27] |
| Zero-shear-rate viscosity, $\eta_0$ (Pa s) | 192.5 @ 250 °C | 168 @ 290 °C [27] |
| Ratio of solvent to zero-shear-rate viscosity, $\beta$ | 0.3 | 0.0954 [27] |
| Ziabicki maximum crystallization rate, $K_{max}$ (1/s) | 1.64[a] | 1.64 [27] |
| Ziabicki maximum crystallization temperature, $T_{max}$ (K) | 407[a] | 423 [27] |
| Equilibrium melting temperature, $T_{m0}$ (K) | 493 [23] | 537 [27] |
| Ziabicki crystallization half-width, $T_D$ (K) | 91[a] | 91[b] [29] |
| Intrinsic amorphous birefringence, $\Delta\alpha_i$ | 0.09[a] | 0.09 [27] |
| Stress-optical coefficient, $C_{op}$ (m$^2$/N) | $1.3\times10^{-9}$[a] | $1.3\times10^{-9}$ [27] |
| Stress-crystallization coupling coefficient, $C$ | 52[a] | 52 [29] |
| Dimensionality of growth (Avrami index), $n$ | 1 | 1 |
| Heat of fusion, $\Delta H_f$ (J/kg) | $-1.88406\times10^5$[a] | $-1.88406\times10^5$ [27] |
| Ultimate DOC, $\varphi_\infty$ | 0.4 | 0.45 [27] |
| Friction coefficient ratio, $\zeta_\perp/\zeta_{\parallel}$ | – | 10 to 1000[c] [29] |
| Order of orientation to entropy coupling, $m$ | – | 2 to 50[c] [29] |
| Melting temperature at perfect alignment, $T_{m\infty}$ (K) | – | 560 to 1500[c] [29] |
| Glass transition temperature, $T_g = T_\infty$ (K) | 320 | 318 [27] |
| Nucleation pre-factor, $N_0$ (m$^{-3}$) | – | $3.33\times10^{16}$ [29] |
| Crystal rod cross-sectional area, $A_f$ (m$^2$) | – | $3.14\times10^{-16}$ [29] |
| Growth pre-factor, $G_0$ (m/s) | – | 2.415 [29] |
| Equilibrium activation energy of motion, $U_0^*/R$ (K) | – | 125 [29] |
| Primary surface nucleation constant, 3 ($\kappa_T - \kappa_G$) | – | 0.096 [29] |
| Secondary surface nucleation constant, $\kappa_G$ | – | 0.235 [29] |
| WLF parameter $C_1$ | 1.8[a] | 1.8 [43] |
| WLF parameter $C_2$ (K) | 295[a] | 295 [43] |

[a] Due to the lack of data, these properties were estimated based on the corresponding values for Nylon-6,6, and are within typical reported ranges [47]. Calculations are not very sensitive to the estimated parameters, with the exception of the stress-crystallization coupling coefficient, $C$.
[b] Crystallization half-width was modified from the typical value of 313 K to match the Kolmogoroff model with its corresponding parameters. See text for discussion.
[c] Several combinations of these parameters are used. Further experimental data is needed. See Results section for discussion.

Nylon-6,6. The Arrhenius and WLF shift factors with parameters from Table 1 are compared in Fig. 4.

## 4. Results and discussion

Electrospinning is an effective method to produce sub-micron scale fibers – nanofibers. Such fibers are relatively easy to obtain from polymer solutions, where about an order of magnitude thinning can be obtained solely due to solvent evaporation. It is significantly more difficult to obtain nanofibers from melt, and careful process optimization is required. The theoretical model development and simulation efforts provide the needed guidance to effective process optimization. The fundamental process

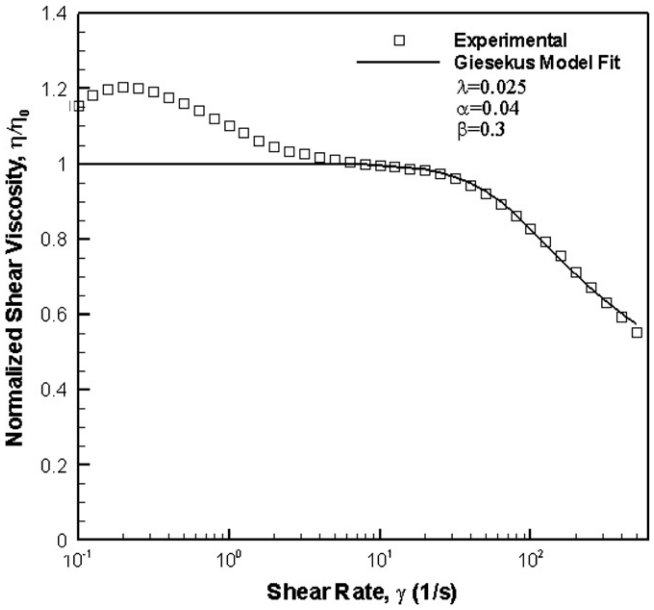


**Fig. 2.** Fit of the Nylon-6 rheological data at 250 °C to the Giesekus constitutive model.

understanding gained in the present study has helped in the recent success of achieving sub-micron Nylon-6 fibers from melt, Fig. 5.

We note that for the stable jet model validation studies included in this paper, different conditions are used. The jet is quenched to prevent the whipping motion, not accounted for in the model. The larger fiber diameters also simplify the jet imaging. Even though the fibers used in this work are thicker, the findings are relevant to the nanofiber spinning process. An optimized stable jet will set the stage for the optimized overall process.

In this section, the present polymer melt electrospinning model coupled with crystallization equations for Nylon-6 will be validated with experimental results. Then, the qualitative behavior of the crystallization model compared to the Ziabicki model will be explored. Finally, the new FIC model will be applied to the study of electrospinning of Nylon-6,6.

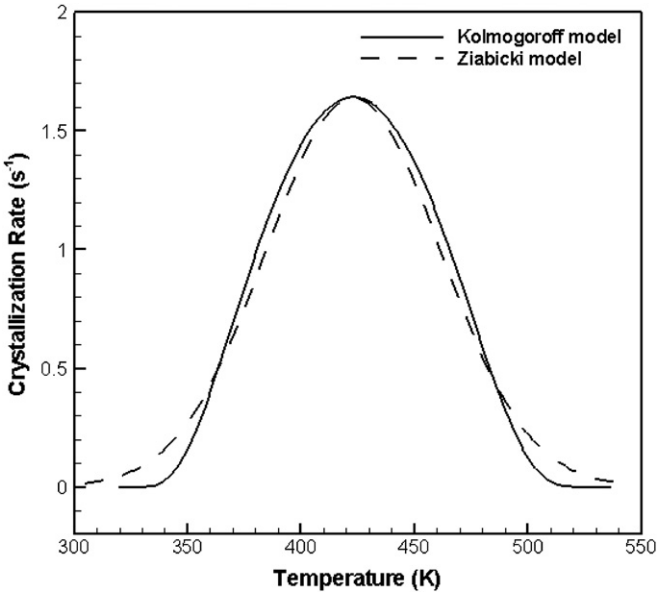


**Fig. 3.** Quiescent crystallization rate of Nylon-6,6 for Kolmogoroff and Ziabicki models.

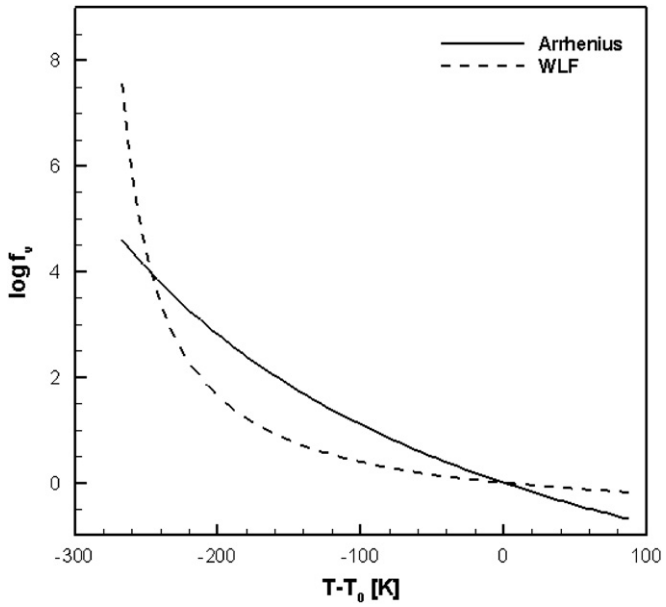


**Fig. 4.** Comparison of rheological shift factors for Nylon-6,6 computed using Arrhenius and WLF relationships. $T_0$ is the reference temperature at which the zero-shear-rate viscosity and the relaxation time were determined (ideally, it is the melt temperature at the nozzle).

### 4.1. Validation of non-isothermal polymer melt electrospinning model for Nylon-6

In a previous publication [37], the electrospinning model has been validated by comparing the simulation predictions to initial thinning and final jet diameters of electrospun PLA melt. In this work, the FIC model by Ziabicki was incorporated into non-isothermal modeling of melt electrospinning, and the corresponding results for Nylon-6 melt are shown. Experiments were carried out using two spinneret sizes to explore the range of applicability of the present model. The experimental conditions used in these studies are summarized in Table 2.

In Fig. 6(a), the experimental initial thinning profile obtained using a 17 gauge needle with inner radius of 0.52 mm is compared to predictions of four variants of the model: i) Giesekus constitutive model with Arrhenius rheological shift factor, ii) Giesekus model with WLF shift factor, iii) PTT model with Arrhenius shift factor, and iv) PTT model with WLF shift factor. All variants show good agreement with experiment. The similarity of predictions for the

**Table 2**
Experimental conditions for Nylon-6 electrospinning.

| Parameters | 17 gauge needle case | 22 gauge needle case |
|---|---|---|
| Needle radius, $R_0$ (mm) | 0.52 | 0.205 |
| Flow rate, $Q$ (ml/min) | 0.02 | 0.003–0.02 |
| Melt (nozzle) temperature, $T_0$ (K) | 518 | 533–573 |
| Cooling air temperature, $T_\infty$ (K) | 298 | 298 |
| Applied potential, $\Delta V$ (kV) | 20 | 28 |
| Distance between electrodes, $d$ (m) | 0.1 | 0.1 |

Giesekus and PTT constitutive models in the initial thinning region is due to relatively small internal stresses; in this limit, the predictions of the two models are expected to converge. The overlap in the Arrhenius and WLF implementations is due to that the temperatures in this region do not significantly depart from the inlet (reference) temperature. WLF results in slightly thinner jets, as the shift factor here is fractionally smaller than the Arrhenius counterpart (see Fig. 4). As the temperature drops further in the downstream region, the WLF shift factor takes a sharp upturn, however no significant thinning occurs in that region, and thus this does not result in relative fiber thickening.

In Fig. 6(b), the predicted initial jet profiles are compared to experimental data obtained for thinner 22 gauge needle with inner radius of 0.205 mm at three different melt temperatures. These smaller needle studies presented some difficulties to accurately and precisely control the experimental conditions. It was observed that the jet shape remained constant for various flow rate settings. It is hypothesized that high melt viscosity and small needle size caused a large pressure drop, and this increased resistance to flow limited the flow rate to some value smaller than the set point. Therefore, for the presented model results, flow rate was taken as an adjustable parameter. The fits were obtained by starting with the experimental set point flow rate – 0.05 ml/min, and then decreasing it until acceptable fits of the radius profiles were obtained. For high temperature cases, the viscosity and therefore resistance to flow was the smallest, so the fitted flow rate was closest to the experimental set point.

The final fiber diameters predicted by the stable jet model, using Giesekus constitutive model and Arrhenius rheological shift factor, agree well with the experimental measurements on the collected melt-electrospun Nylon-6 fiber mats, as shown in Fig. 7. The deviation at high melt temperature for the 17 gauge needle case is due to the whipping instabilities that could not be completely suppressed in this experiment. The whipping motion resulted in a drastically increased jet flight path and additional thinning, which

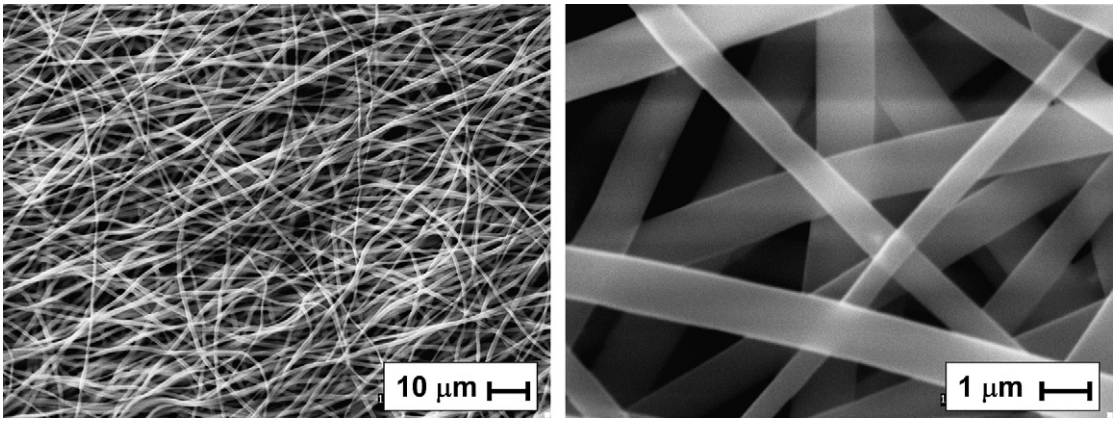


**Fig. 5.** SEM images of sub-micron electrospun Nylon-6 fibers.

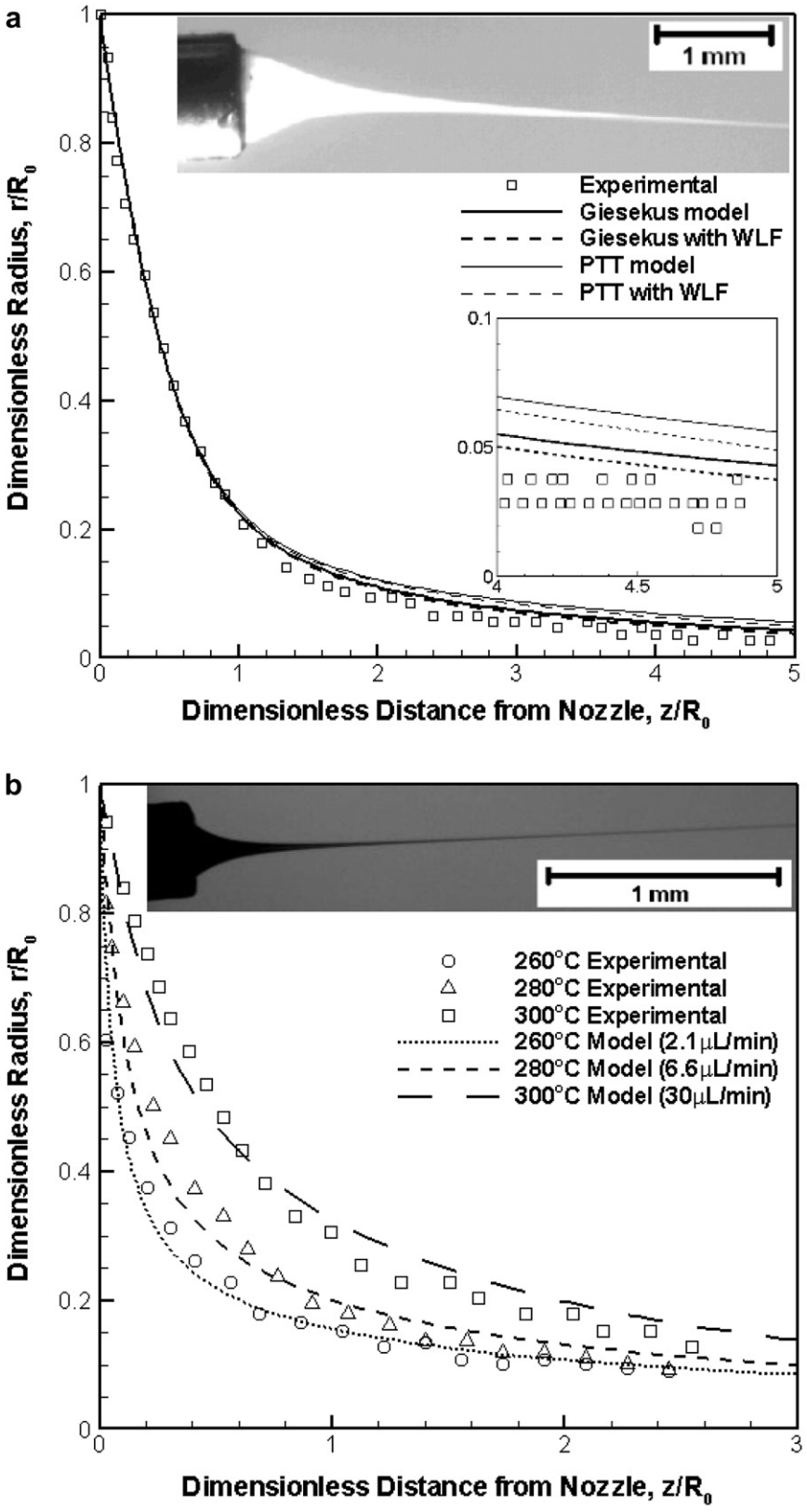


**Fig. 6.** Initial radius profiles for electrospinning of Nylon-6 melt with a) 17 gauge and b) 22 gauge needle.

was not accounted for by the present model. This indicates that sub-micron Nylon fibers can be readily obtained from melt electrospinning by proper control of the ambient temperature in the spinning region. The effect of in-flight crystallization on the final jet diameter is not very significant in the low melt temperature cases. We will show in the next section that this is due to practically decoupled transport and crystallization phenomena. The onset of FIC will be observed only after the completion of the initial fast jet

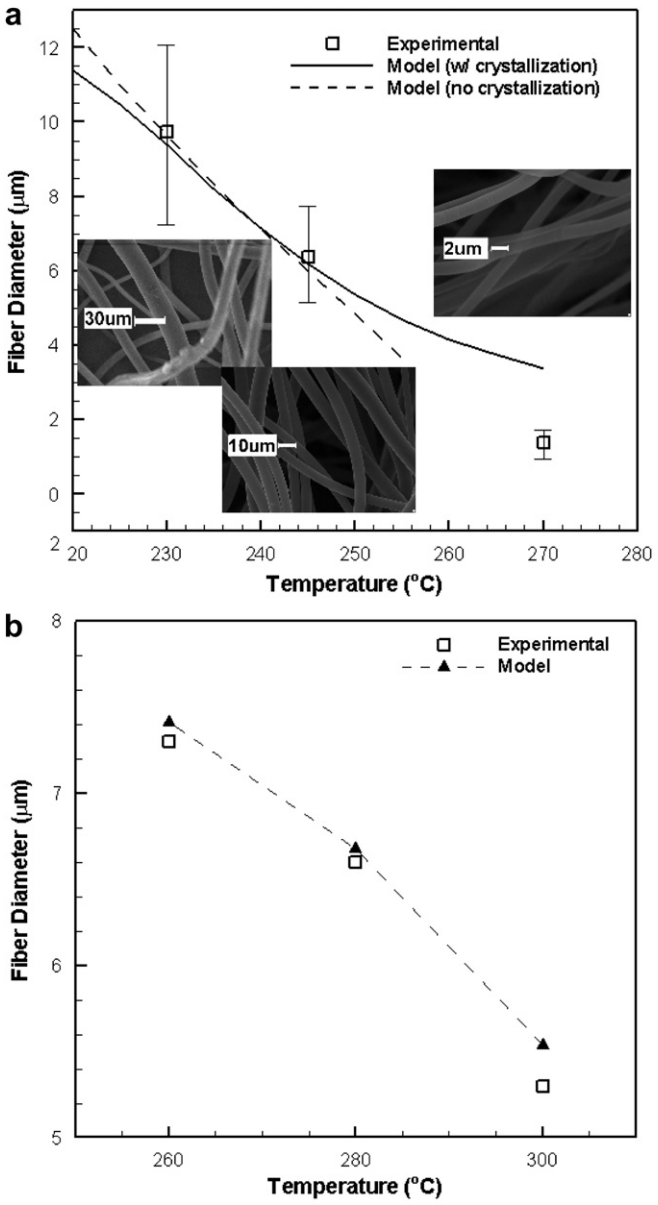


**Fig. 7.** Final diameters of fibers electrospun from Nylon-6 melt with: a) 17 gauge and b) 22 gauge needle.

thinning stage. However, this will not necessarily be the case for other materials of interest. Another interesting feature is the crossover in the two model curves at about 240 °C. As will be seen in the next section, this point corresponds to the onset of the rapid FIC. Hence, the crossover can be attributed to competition of thermal and stress effects of crystallization on the viscosity of the jet. At lower melt temperatures, the viscosity decrease due to release of latent heat of fusion from slow thermal crystallization dominates. At higher melt temperatures, the thermal effects are overshadowed by a sharp viscosity spike caused by rapid flow-induced phase transition.

For the thin 22 gauge needle cases, higher melt temperatures and smaller initial jet sizes resulted in numerical issues with the model. Rapid jet thinning caused unusually high polymeric stresses and eventually resulted in divergence of solutions. To avoid this issue, the maximum stress derivatives had to be artificially capped, and the cut-off values were based on observations from the 17 gauge needle studies. For the 260 °C case, the corresponding 17 gauge needle maximum stress derivative was adjusted slightly to produce good agreement of the final fiber diameter with the experimental value. For the other temperatures, the cut-off derivatives were determined by empirically scaling the 260 °C cut-off inversely with flow rate. As seen in Fig. 7(b), this procedure resulted in reasonable agreement with experiments. However, the needed adjustments to the model clearly demonstrate its limitations for the small nozzle experiments.

In this section, we have shown that the present model is practically predictive for the large needle cases with no whipping motion, as no fitting parameters have been used. However, for small needle cases, a number of experimental uncertainties were present, and various modifications were required for model to match experimental results. Due to these limitations, further analysis in this work is presented for the 17 gauge needle case only.

### *4.2. Validation of Ziabicki crystallization modeling approach for Nylon-6*

In this section we will concentrate on the coupling behavior of Ziabicki crystallization and transport equations and compare the model predictions with experimental crystallinity measurements. Melt electrospinning of Nylon-6 with a 17 gauge needle will be the benchmark for this study.

Fig. 8 shows the effect of changing the melt temperature at the nozzle on some of the monitored variables in the region close to the spinneret. As in previous studies [37], increasing melt temperature results in faster thinning and higher stresses. The agreement between Giesekus and PTT models with Arrhenius and WLF shift factors remains good, and the trends observed above are maintained. The decrease in the Ziabicki crystallization rate with melt temperature has to do with the temperature in the jet at each corresponding axial position. As seen in Fig. 3, crystallization rate has a nearly Gaussian profile in temperature, and thus higher melt temperatures result in slower thermal crystallization. It should be noted that, although the onset of fast FIC takes place further downstream, when polymer chain orientation approaches perfect alignment in the axial direction, present results reveal that deformation by the strong electric field is very effective, and thus significant molecular orientation is achieved even a few radii away from the nozzle.

We note that in the initial thinning region only limited, thermally-induced crystallization is observed due to elevated temperatures and insufficient polymer chain orientation, and thus crystallization dynamics are of little importance in this region. However, rapid FIC takes place downstream, which has a significant impact on the final fiber diameters, as shown in Fig. 9. Furthermore, rapid chain alignment induced by strong internal stresses reverses the crystallization trend observed in the initial thinning region. Increased melt temperature results in thinner fibers and higher internal stresses, and thus the onset of FIC is the earliest for high melt temperatures. In Fig. 9, only the Giesekus model with Arrhenius rheological shift factor results are shown. This is because the other three cases respond more sharply to internal stresses, and thus suffered from a singularity caused by rapid internal stress buildup in the thin radius and high temperature regimes, as observed in the previous section. The onset of such a singularity is seen for the PTT model profiles at 270 °C in Fig. 8. Further investigations on this phenomenon should be conducted, but one of the possible reasons for the observed behavior is the set of rheological and WLF parameters used in this work.

The experimental crystallization data of Nylon-6 shown in Fig. 10 supports the model predictions. DSC data, using 20 °C/min scanning rate, Fig. 10(a), shows strong crystallization peaks of nearly identical magnitudes. Time integration of these peaks provides an estimate

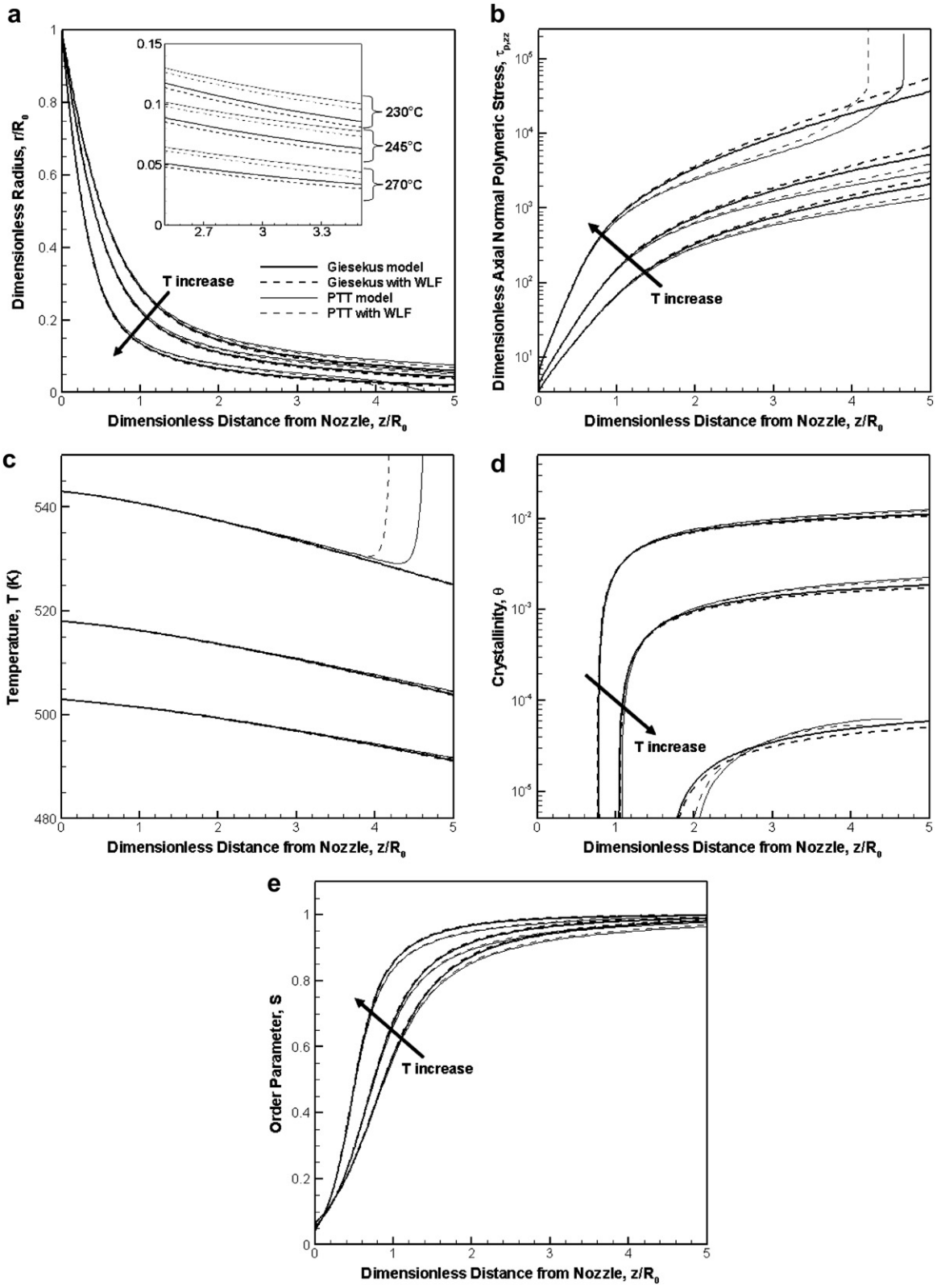


**Fig. 8.** Initial profiles for electrospinning of Nylon-6 using 17 gauge needle at various melt (nozzle) temperature conditions: a) radius, b) axial normal stress, c) temperature, d) crystallinity (note that the *y*-axis scale has been changed to log-scale for illustration purposes), and e) order parameter.

for the DOC, and all experiments result in DOC ≈ 40%, which is close to the maximum achievable crystallinity of Nylon-6 as seen in the DSC of as-received pellets. In general, Nylon-6 can crystallize in $\alpha$ or $\gamma$ forms, the first being the more stable configuration usually achieved under quiescent conditions, and the latter is a metastable structure stabilized by confinement or strong deformation during crystallization. The $\alpha$ form has a higher melting point (above 220 °C) as shown for the case of as-received pellets. The $\gamma$ form has a lower

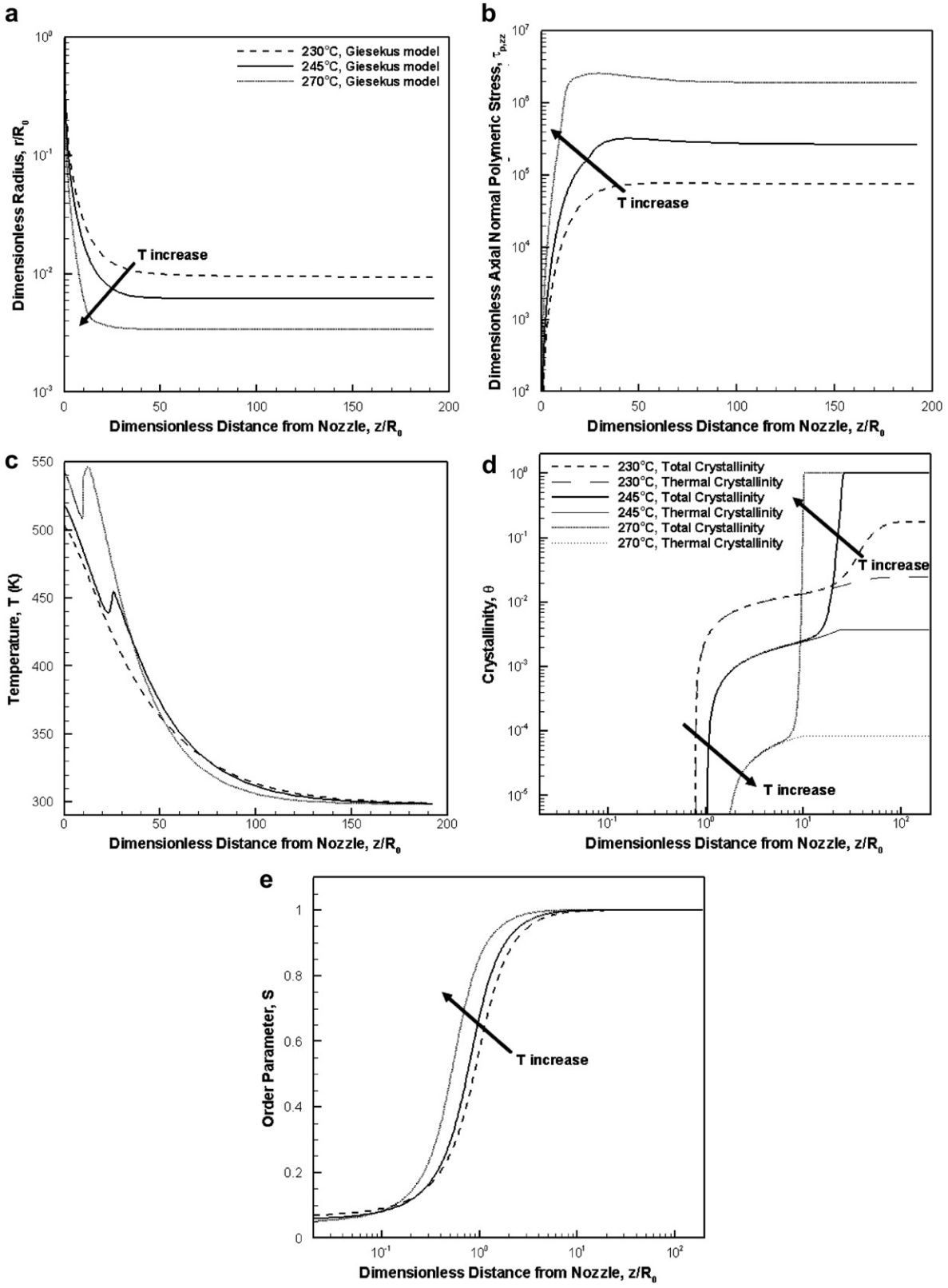


**Fig. 9.** Entire spinning region axial profiles for electrospinning of Nylon-6 with 17 gauge needle: a) radius, b) axial normal stress, c) temperature, d) crystallinity (note that both x- and y-axis scales have been changed to log-scale for illustration purposes), and e) order parameter.

melting point but, as previously reported by Kwak, et al. [24], it can be elevated by further stabilization due to additional confinement and deformation experienced by the polymer. In the case of fibers electrospun from melt at 230 °C, two peaks are observed, indicating presence of both $\alpha$ and $\gamma$ phases. The $\alpha$ phase most likely appears due to secondary crystallization after electrospinning, either on the collector plate or in DSC crucible. Interestingly, this observation qualitatively supports the numerical result of only partial final DOC

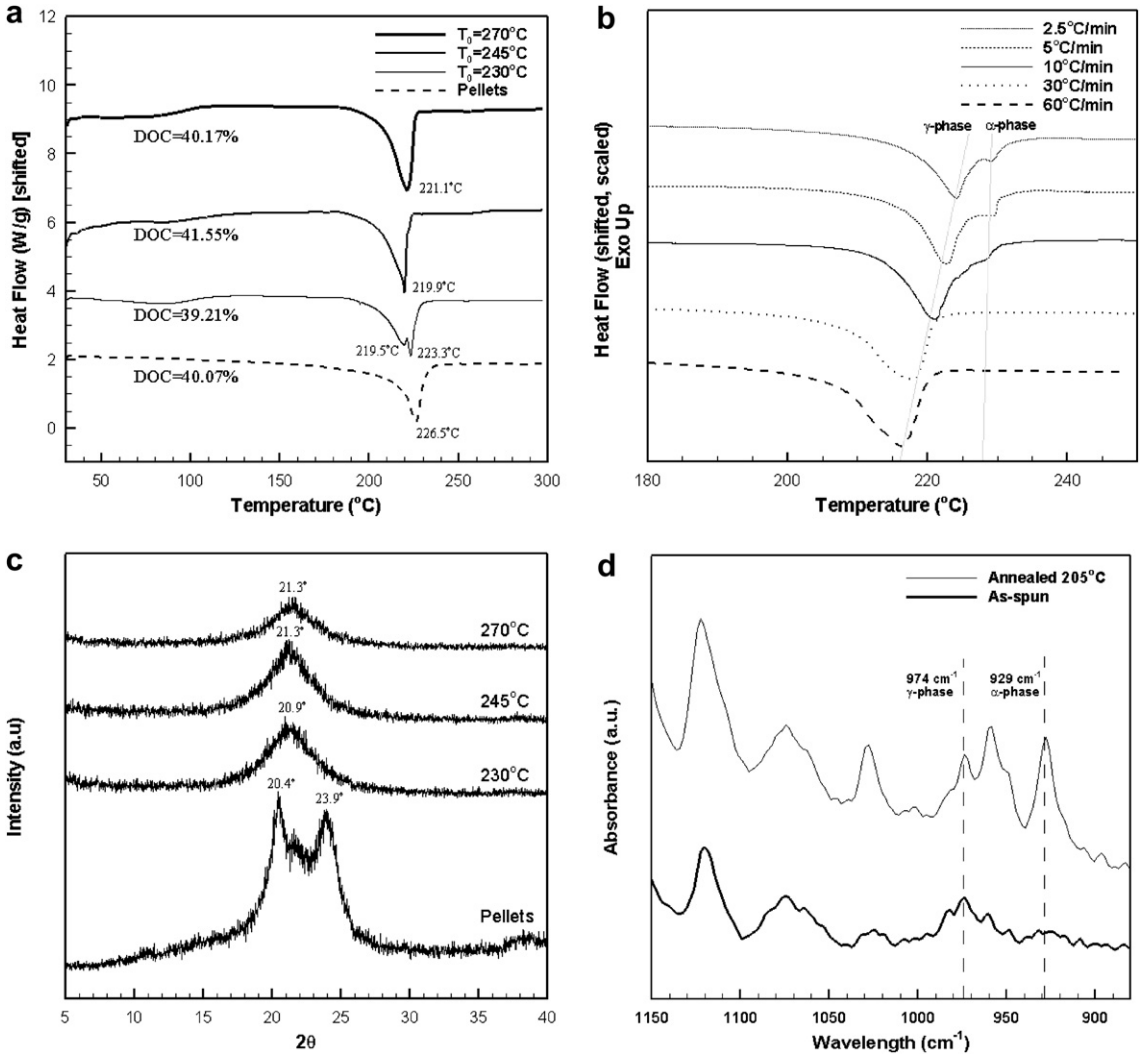


**Fig. 10.** Crystallinity of electrospun Nylon-6 fibers: a) DSC for fibers obtained at various nozzle temperatures, scans done at 20 °C/min in the range of 25–300 °C, b) DSC at various scanning speeds for samples obtained under identical conditions, c) WAXD for fibers obtained at various nozzle temperatures, d) FTIR for as-spun and annealed (at 205 °C for 8 h) fibers. The DOC was calculated as $(\Delta H/\Delta H_f) \times 100\%$, where $\Delta H$ is the area of the crystallization peak, and $\Delta H_f$ is the heat of fusion from Table 1.

for this case (Fig. 9). As the melt temperature is increased to 245 °C and 270 °C, the $\alpha$ peak disappears, suggesting that complete crystallization took place in the electrospinning process, and the $\gamma$ peak is shifted toward higher temperature, as expected, due to deformation-induced metastable phase stabilization. Both of these observations are again in agreement with the simulation results presented in Fig. 9. To confirm that the single peak is in fact due to the stabilized $\gamma$- and not $\alpha$-phase, the DSC scanning rates were varied from 60 °C/min to 2.5 °C/min, Fig. 10(b). At faster scanning speeds, the $\gamma$-phase remained stable and resulted in a single peak. At slower scanning speeds, the $\gamma$-phase had time to partially reorganize and began forming the more stable $\alpha$-phase, which manifested itself in the small peak at ~226 °C.

The WAXD patterns, Fig. 10(c), show a clear distinction between the $\alpha$-phase obtained from quiescent crystallization in as-received pellets (two peaks near 20.5° and 24°), and the $\gamma$-phase of the electrospun fibers (broad peak near 21°). The WAXD patterns can often be used to provide secondary confirmation for the DOC through the ratio of crystalline peaks to the amorphous halo, however, in the case of Nylon-6, the $\gamma$-phase peak overlaps the broad amorphous halo, making the deconvolution process extremely challenging and inaccurate. In future studies, it would be of interest to take a look at two-dimensional WAXD patterns to gain insight into the crystalline morphology, orientation, and radial distribution of crystals in the nanofibers. With further experimental modifications, it should also be possible to take on an on-line measurement of crystallization dynamics during the electrospinning process, *i.e.* measure the axial crystallization profiles for direct comparison to simulations, as done in fiber spinning by Samon, et al. [25].

The most conclusive evidence of the $\gamma$-phase formation in melt electrospinning of Nylon-6 is shown by FTIR spectra, Fig. 10(d). The 974 cm$^{-1}$ peak is a characteristic marker of the $\gamma$-phase [26]. It is also seen that the $\alpha$-phase marker at 929 cm$^{-1}$ is not present in the as-spun fibers, but is evident in the annealed (at 205 °C for 8 h) structures.

In this work, experimental confirmation of the initial thinning dynamics has been provided through high speed imaging of the jet profile. The model predictions were also compared to fiber sizes and their crystallinity in the collected fiber mats. To obtain further experimental confirmation, thermal measurements using high resolution infrared camera are currently underway. The online crystallization measurement requires extensive setup modifications, and is planned for future studies.

### 4.3. The new crystallization model trends and behavior in the bulk

The behavior of the newly-developed FIC model is explored by comparing the predictions to the Ziabicki FIC model, using Nylon-6,6 as a model polymer. The goal of this work is to show that the present model is capable of capturing similar qualitative behavior in the overall DOC profiles under various conditions.

In isothermal crystallization, Fig. 11(a), a second-order coupling of orientation and entropy is used, $m = 2$. The friction coefficient ratio was set to $\zeta_{\perp}/\zeta_{||} = 2$, which is a constant value reported for bulk motion of rod-like particles [49]. The melting temperature at perfect alignment is an adjustable parameter, and is optimized to $T_{m\infty} = 560$ K for the case of $S = 0.944$, which is on the order of the typical alignment necessary to observe FIC. However, when the stress level and thus the degree of alignment is decreased to $S = 0.907$, the model with the given parameter set over-predicts the crystallization rate compared to the Ziabicki counterpart. This is because only the importance of short range order is considered ($m = 2$). The agreement is improved as the order (range) of the interactions is increased to $m = 50$, but for each new value of $m$, a new value of the melting point $T_{m\infty}$ has to be determined. Each $\{m, T_{m\infty}\}$ set is obtained by achieving a perfect fit at $S = 0.944$, resulting in the values shown in Table 3. It can be observed that the long range order requirement forces a drastic increase in the melting point of a perfectly aligned structure, $T_{m\infty}$. Thus, we note that while this quantity is given a physical interpretation, and the correctness of the large or even infinite values may be argued, it may also remain a "fictive" and idealistic model parameter. In this study, the idea was to consider a range of parameters, from more "classical" values to a hypothetical extreme case, and the acceptable range for the values of $T_{m\infty}$ remains to be determined by dedicated molecular scale investigations.

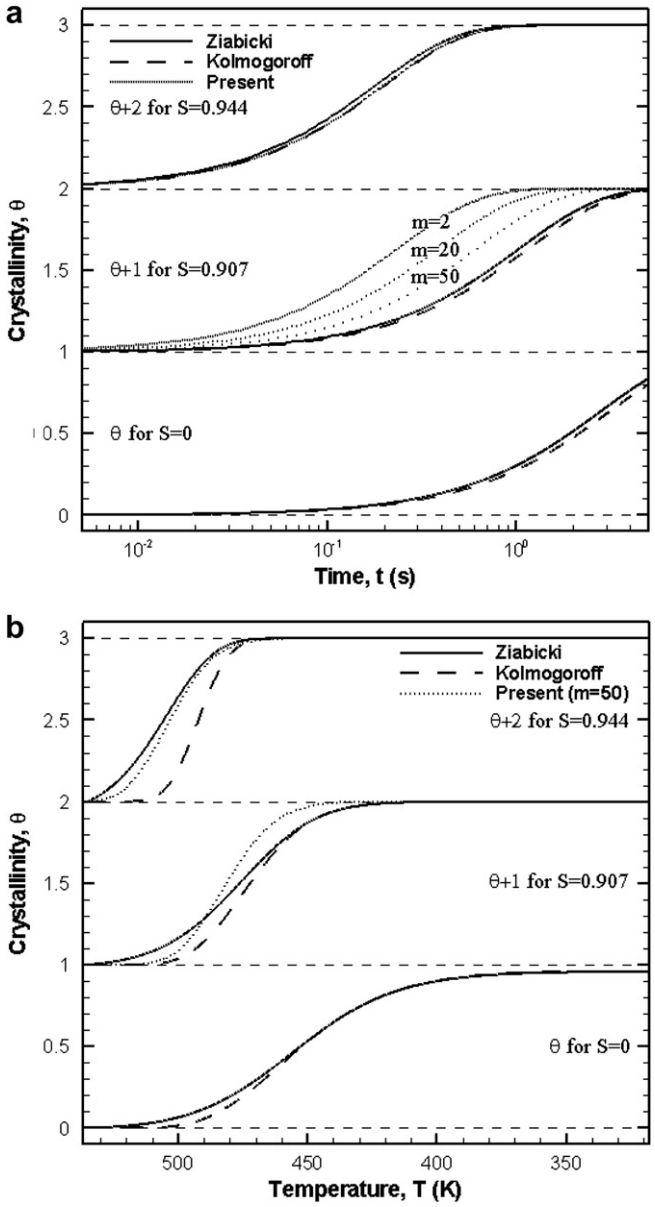


**Fig. 11.** Crystallization of Nylon-6,6 in the bulk: (a) isothermally at 490 K, and (b) non-isothermally with 50 K/s cooling. NOTE: At $S = 0$, the present model reduces to the classical Kolmogoroff model, Equation (7). At $S > 0$, by Kolmogoroff model we mean the classical quiescent model, modified with the Ziabicki stress enhancement factor (second exponent in Equation (3)).

**Table 3**
Optimized sets of parameters for crystallization of Nylon-6,6 in the bulk.

| $m$ | $T_{m\infty}$ |
|---|---|
| 2 | 560 K |
| 20 | 610 K |
| 50 | 1500 K |

Using the parameters obtained from isothermal studies, the model predictions are verified under non-isothermal conditions, Fig. 11(b), and a reasonable agreement between the models is observed. Based on this initial FIC model validation, we can proceed to its implementation in the electrospinning simulations, as discussed in the following section.

### 4.4. Crystallization in electrospinning of Nylon-6,6

The new FIC model is incorporated into the previously developed [37] non-isothermal simulation of polymer melt electrospinning using the parameters in Table 1 and experimental conditions shown in Table 4.

In the present study, only results based on the Giesekus constitutive model with the Arrhenius rheological shift factor are included, as this approach is less prone to the singularities experienced when the PTT model and/or the WLF equation are applied. These models have been investigated and similar trends to those reported above are observed. Fig. 12 shows the axial profiles of various characteristics of the Nylon-6,6 jet. A reasonable agreement between the Ziabicki and the present FIC models is observed. In fact, as opposed to the bulk studies, high values of $m$ are not required to reasonably capture the crystallization behavior predicted by Ziabicki, since the order parameter evolution is extremely rapid in electrospinning. However, for electrospinning simulations, the value of the friction coefficient ratio, $\zeta_{\perp}/\zeta_{||}$, had to be increased from its bulk value to account for the geometric confinement effects, as shown in Table 5. The polymer melt jets in electrospinning are not thin enough to produce atomistic level

**Table 4**
Experimental parameters for Nylon-6,6 electrospinning.

| Parameters | |
|---|---|
| Needle radius, $R_0$ (mm) | 0.52 |
| Flow rate, $Q$ (ml/min) | 0.044 |
| Melt (nozzle) temperature, $T_0$ (K) | 593 |
| Cooling air temperature, $T_\infty$ (K) | 298 |
| Applied potential, $\Delta V$ (kV) | 20 |
| Distance between electrodes, $d$ (m) | 0.1 |

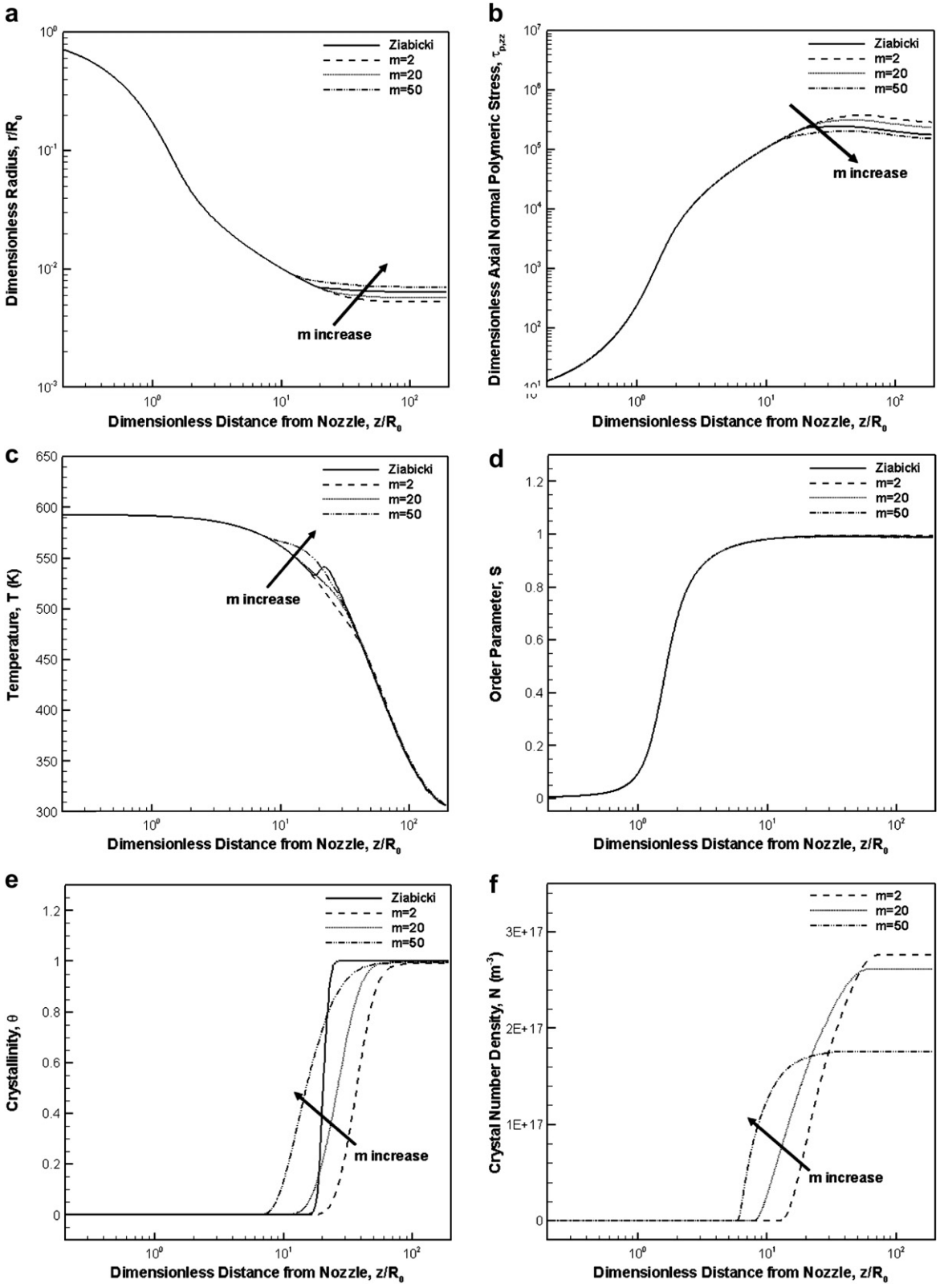


**Fig. 12.** Entire spinning region axial profiles for electrospinning of Nylon-6,6 using Ziabicki and the present FIC models (note that the *x*-axis scales have been changed to log-scale for all plots for illustration purposes): a) radius, b) axial normal stress, c) temperature, d) order parameter, e) crystallinity, and f) crystal number density.

confinement, which would drastically affect the flow and crystallization dynamics and furthermore challenge the validity of the continuum level treatment. However, long polymeric chain motion is hindered, especially in the crystallization region where fiber diameters are on the order of 10 μm. The effects of confinement on the motion of rod-like elements in thin films have been studied in the past [49], and increases of friction coefficient ratios by an order of magnitude were common. In the present case, there is an

**Table 5**
Optimized sets of crystallization parameters for Nylon-6,6 in electrospinning.

| $m$ | $T_{m\infty}$ | $\zeta_{\perp}/\zeta_{\|\|}$ |
|---|---|---|
| 2 | 560 K | 1000 |
| 20 | 610 K | 50 |
| 50 | 1500 K | 10 |

additional degree of confinement (from thin films to thin jets), thus the entire range of the values reported in Table 5 should be reasonable.

It has been shown that the present model can capture the crystallization behavior predicted by the Ziabicki model. The jet radius, stress, order parameter, temperature, and crystallization profiles are not extremely sensitive to the particular values of the three parameters used by the model, as long as their combination is self-consistent. In addition, the present model provides some additional microstructure information, *e.g.*, the number of crystals and their sizes, which are seen to be strong functions of the particular model parameters. This suggests that additional information has to be collected to determine the parameter values independently. For example, the friction coefficient ratio can be found from further computational analysis on the rod motion in a one-dimensional confined geometry, and appropriate $\{m, T_{m\infty}\}$ sets can be found from experimental studies of crystallization under deformation in the bulk or even further computational work. Thorough experimental model validation would include on-line crystallization measurement to provide axial crystallinity profiles, as well as an optical light scattering measurement to elucidate the crystallite density based on the number of grain boundaries.

The current work has demonstrated the flexibility of the new FIC model, which can provide microstructure information such as crystallite number density and average size, and utilizes parameters that have precise physical meanings. However, the FIC phenomenon is extremely complex and both computationally and experimentally challenging, and further detailed studies and experimental validation are underway. The more complex issues of crystalline phase morphology formation and evolution in FIC remain to be addressed. These phenomena are unlikely to be accurately described by continuum level models alone and will require some level of mesoscale or molecular scale treatment and possibly multi-scale simulation.

## 5. Conclusions

A model for the stable jet region in electrospinning of crystallizing polymer melts has been presented and its predictions validated with experimental data on Nylon-6. Good agreement between the model and the experimental data at hand was noted and additional experiments for further validation have been proposed. In particular, it is important to provide confirmation of the transient behavior (temperature and crystallinity evolution) via on-line experimental measurements.

A new FIC model that will provide microstructure information (crystallite number density and average size) has been proposed. The model parameters have precise physical meanings and can be obtained from experiments or further micro scale modeling. The model trends and behavior under isothermal and non-isothermal conditions in the bulk have been investigated and showed good agreement with the widely-used Ziabicki model. The equations were also coupled with the electrospinning model to study the confinement effects of the thin jets. Nylon-6,6 was used as the model polymer in this study and the results were again in agreement with the Ziabicki model. A number of further experimental confirmation studies are currently underway.

## Acknowledgements

The authors would like to thank the National Science Foundation for funding this work through CAREER Award to Prof. Joo, Grant no. CTS-0448270. We would also like to thank E.I. du Pont de Nemours and Company for funding through DuPont Young Professor Grant to Prof. Joo.

## References

[1] Rocha IS, Malmonge LF, Mattoso LHC, Malmonge LF, Gregorio Jr R. Effect of low contents of a polyaniline derivative on the crystallization and electrical properties of blends with PVDF. J Polym Sci Part B 1999;37:1219–24.
[2] D'Alkaine CV, Otaguro H. The effect of step isothermal crystallization on the polymer crystalline morphology: the case of isotactic polystyrene. Polimeros: Ciencia e Tecnologia 2001;11:234–9.
[3] Schneider HA. Flexibility and phase transitions of polymers. J Appl Polym Sci 2003;88:1590–9.
[4] Sliwinska-Bartkowiak M, Dudziak G, Sikorski R, Gras R, Radhakrishnan R, Gubbins K. Melting/freezing behavior of a fluid confined in porous glasses and MCM-41: dielectric spectroscopy and molecular simulation. J Chem Phys 2001;114:950–62.
[5] Kimura T, Maruyama S. Molecular dynamics simulation of heterogeneous nucleation of a liquid droplet on a solid surface. Micro Thermophys Eng 2002;6:3–13.
[6] Ma J, Zhang S, Qi Z, Li G, Hu Y. Crystallization behaviors of polypropylene/montmorillonite nanocomposites. J Appl Polym Sci 2002;83:1978–85.
[7] Toxvaerd S. Heterogeneous nucleation at a planar surface. Physica A 2002;314:442–7.
[8] Brereton GJ, Crilly RJ, Spears JR. Nucleation in small capillary tubes. Chem Phys 1998;230:253–65.
[9] Koscher E, Fulchiron R. Influence of shear on polypropylene crystallization: morphology development and kinetics. Polymer 2002;43:6931–42.
[10] Kolmogoroff AN. On the statistical theory of the crystallization of metals. Isv Akad Nauk SSSR Ser Math 1937;1:355–9.
[11] Avrami M. Kinetics of phase change: I, II, III. J Chem Phys 1939;7:1103–12. 8, 212–224(1940); 9, 171–184 (1941).
[12] Eder G. Mathematical modeling of crystallization processes as occurring in polymer processing. Nonlinear Anal Theo Meth Appl 1997;30:3807–15.
[13] Ozawa T. Kinetics of non-isothermal crystallization. Polymer 1971;12:150–8.
[14] Nakamura K, Katayama K, Amano T. Some aspects of nonisothermal crystallization of polymers. II. Consideration of the isokinetic condition. J Appl Polym Sci 1973;17:1031–41.
[15] Ziabicki A. Fundamentals of fiber formation. New York: Wiley; 1976.
[16] Lauritzen Jr JI, Hoffman JD. Theory of formation of polymer crystals with folded chains in dilute solution. US Bur Standards – J Res Phys Chem 1960;64A:73–102.
[17] Urbanovici E, Schneider HA, Cantow HJ. Some considerations concerning the temperature dependence of the bulk crystallization rate constants of polymer materials. J Polym Sci B, Polym Phys 1997;35:359–69.
[18] Becker R, Döring W. Kinetic treatment of grain-formation in super-saturated vapours. Ann Phys 1935;24:719–52.
[19] Ko MJ, Waheed N, Lavine MS, Rutledge GC. Characterization of polyethylene crystallization from an oriented melt by molecular dynamics simulation. J Chem Phys 2004;121:2823–32.
[20] Kumaraswamy G, Issaian AM, Kornfield JA. Shear-enhanced crystallization in isotactic polypropylene, 1: correspondence between in situ Rheo-optics and ex situ structure determination. Macromolecules 1999;32:7537–47.
[21] Kumaraswamy G, Kornfield JA, Yeh F, Hsiao BS. Shear-enhanced crystallization in isotactic polypropylene, 3: evidence for a kinetic pathway to nucleation. Macromolecules 2002;35:1762–9.
[22] Shin DM, Lee JS, Jung HW, Hyun JC. High-speed fiber spinning process with spinline flow-induced crystallization and neck-like deformation. Rheol Acta 2006;45:575–82.
[23] Liu Y, Cui L, Guan F, Gao Y, Hedin NE, Zhu L, et al. Crystalline morphology and polymorphic phase transitions in electrospun Nylon-6 nanofibers. Macromolecules 2007;40:6283–90.
[24] Kwak SY, Kim JH, Kim SY, Jeong HG, Kwon IH. Microstructural investigation of high-speed melt-spun Nylon 6 fibers produced with variable spinning speeds. J Polym Sci B, Polym Phys 2000;38:1285–93.
[25] Samon JM, Schultz JM, Wu J, Hsiao B, Yeh F, Kolb R. Study of the structure development during the melt spinning of Nylon 6 fiber by on-line wide-angle synchrotron X-ray scattering techniques. J Polym Sci B, Polym Phys 1999;37:1277–87.
[26] Lee K-H, Kim K-W, Pesapane A, Kim H-Y, Rabolt JF. Polarized FT-IR study of macroscopically oriented electrospun Nylon-6 nanofibers. Macromolecules 2008;41:1494–8.

[27] Joo YL, Sun J, Smith MD, Armstrong RC, Brown RA, Ross RA. 2-D numerical analysis of non-isothermal melt spinning with and without phase transition. J Non-Newt Fluid Mech 2002;102:37–70.
[28] Doufas AK, Dairanieh IS, McHugh AJ. A continuum model for flow-induced crystallization of polymer melts. J Rheol 1999;43:85–109.
[29] Zhmayev E, Joo YL. Modeling of crystallizing polymer melts in electrospinning. AIP Conf Proc 2008;1027:9–11.
[30] Fong H, Reneker DH. 6. electrospinning and the formation of nanofibers. In: Salem DR, editor. Structure formation in polymeric fibers. Munich: Hanser Gardner Publications; 2001. p. 225–46.
[31] Li BD, Xia Y. Electrospinning of nanofibers: reinventing the wheel? Adv Mater 2004;16:1151–70.
[32] Carroll CP, Joo YL. Electrospinning of viscoelastic boger fluids: modeling and experiments. Phys Fluids 2006;18(053102).
[33] Larrondo L, Manley SJ. Electrostatic fiber spinning from polymer melts. I. Experimental observations on fiber formation and properties, II. Examination of the flow field in an electrically driven jet, III. Electrostatic deformation of a pendant drop of polymer melt. J Polym Sci: Polym Phys Ed 1981;19:909–40.
[34] Lyons J, Li C, Ko F. Melt-electrospinning part I: processing parameters and geometric properties. Polymer 2004;45:7597–603.
[35] Zhou H, Green TB, Joo YL. The thermal effects on electrospinning of Polylactic acid melts. Polymer 2006;47:7497–505.
[36] Carroll CP, Zhmayev E, Kalra V, Joo YL. Nanofibers from electrically driven viscoelastic jets: modeling and experiments. Korea-Aust Rheol J 2008;20:153–64.
[37] Zhmayev E, Zhou H, Joo YL. Modeling of non-isothermal polymer jets in melt electrospinning. J Non-Newt Fluid Mech 2008;153:95–108.
[38] Dzenis Y. Spinning continuous fibers for nanotechnology. Science 2004;304:1917–9.
[39] Ellison CJ, Phatak A, Giles DW, Macosko CW, Bates FS. Melt blown nanofibers: fiber diameter distributions and onset of fiber breakup. Polymer 2007;48:3306–16.
[40] Lamberti G. A direct way to determine IPP density nucleation from DSC isothermal measurements. Polym Bull 2004;52:443–9.
[41] Bird RB, Curtiss CF, Armstrong RC, Hassager O. Dynamics of Polymeric Liquids, Kinetic Theory, vol. 2. , New York: Wiley; 1987.
[42] Zhou H, Kim KW, Giannelis EP, Joo YL. Nanofibers from poly (L-latic) acid nanocomposites: effects of nanoclay on molecular structures. Polymeric Nanofibers. ACS Symposium Series Book, vol.918; 2006. p. 217–30.
[43] Van Meerveld J, Hütter M, Peters GWM. Continuum model for the simulation of fiber spinning, with quiescent and flow induced crystallization. J Non-Newt Fluid Mech 2008;150:177–95.
[44] Larson RG. Constitutive equations for polymer melts and solutions. Boston: Butterworths; 1988.
[45] Patel RM, Bheda JH, Spruiell JE. Dynamics and structure development during high-speed melt spinning of Nylon-6. Part II. Mathematical modeling. J Appl Polym Sci 1991;42:1671–82.
[46] Press WH, Teukolsky SA, Vetterling WT, Flannery BP. Numerical recipes in C: the art of scientific computing. 2nd ed. Cambridge: Cambridge U. Press; 1992.
[47] Overview of materials for Nylon 6, unreinforced, www.MatWeb.com [accessed 07.09.08].
[48] Dielectric constant, strength, and loss tangent, www.RFcafe.com [accessed 07.15.08].
[49] Levine AJ, Liverpool TB, MacKintosh FC. Mobility of extended bodies in viscous films and membranes. Phys Rev E 2004;69(0215503).